Chemical Science

ROYAL SOCIETY OF CHEMISTRY

EDGE ARTICLE

View Article Online
View Journal | View Issue

Cite this: *Chem. Sci.*, 2025, **16**, 13057

All publication charges for this article have been paid for by the Royal Society of Chemistry

Valence state engineering in multi-heteroatom-doped PAHs: a strategy for tunable photophysical properties and phototheranostic potentials†

Yao Ma,‡[a] Dongxu Li,‡[a] Xin Chen,‡[b] Xinqiang Hua,[a] Cheng-Shan Yuan,[a] Jianguo Wang,*[b] Zitong Liu,[a] Hao-Li Zhang[a] and Xiangfeng Shao*[a]

Precise modulation of the electronic structures in heteroatom-doped polycyclic aromatic hydrocarbons (hetero-PAHs) is essential for advancing organic optoelectronic materials. Herein, we report a facile synthetic strategy for hetero-PAHs co-doped with N, O, and S/Se, achieved *via* acid-catalyzed Pictet–Spengler reactions and thermally induced *ipso*-substitution. Systematic π-extension results in a large redshift in optical absorption/emission and enhances fluorescence quantum yield (Φ_F) from 4.0% to 30.5%. Furthermore, a post-synthetic valence state engineering approach enables precise tuning of photophysical properties: (i) oxidation of thiophene units to thiophene *S*,*S*-dioxides increases Φ_F to 42.3% and enhances singlet oxygen generation, and (ii) pyridinium-functionalized hetero-PAHs exhibit strong near-infrared absorption, leading to high photothermal conversion efficiency (up to 61%) at the molecular level. Notably, Se-doped derivatives outperform their S-doped counterparts, underscoring the heavy-atom effect in triplet-state modulation. This work provides a versatile platform for tailoring hetero-PAH electronic structures *via* valence state manipulation, offering potential applications for organic electronics and phototheranostics.

Received 17th March 2025
Accepted 16th June 2025

DOI: 10.1039/d5sc02061a

rsc.li/chemical-science

Introduction

Organic optoelectronic materials have garnered significant attention due to their potential in the development of flexible optoelectronic devices and their inherent biocompatibility, which facilitates applications in biological systems. Among these materials, polycyclic aromatic hydrocarbons (PAHs) have emerged as indispensable building blocks owing to their highly tunable electronic structures and versatile synthetic accessibility.[1] Expanding the π-conjugated framework of PAHs effectively induces bathochromic shifts in both absorption and photoluminescence, particularly extending into the near-infrared (NIR) region, which is highly desirable for bioimaging and photothermal applications.[2]

Beyond extending conjugation, the incorporation of heteroatoms into PAH scaffolds represents a powerful strategy to tailor their geometric and electronic structures, modulate charge transport and photophysical properties, and introduce novel functionalities, thereby broadening their applicability across various domains.[3] Nitrogen is among the most widely utilized heteroatoms for PAH doping, yielding N-doped PAHs with outstanding optical and charge-transport properties.[4] Meanwhile, chalcogen-doped PAHs (incorporating O, S, Se, or Te) have attracted considerable interest in crystal engineering and materials science.[5,6] When multiple heteroatoms are simultaneously introduced into the frameworks of PAHs, their differences in electronegativity, valence states, and atomic radii further enrich the electronic properties, leading to enhanced light absorption, charge separation and transport, and energy conversion efficiencies.[7] Notably, the incorporation of heavy atoms into organic dyes promotes intersystem crossing (ISC), thereby boosting singlet oxygen ($^1O_2$) generation and photothermal conversion efficiency, which are crucial for applications in photodynamic and photothermal therapies.[8]

In addition to heteroatom doping, modulating the valence states of heteroatom dopants provides an effective approach to fine-tune the optoelectronic properties of hetero-PAHs. For instance, in thiophene-containing hetero-PAHs, oxidation of the thiophene units to thiophene *S*,*S*-dioxides significantly enhances photoluminescence quantum yields[9] and induces a transition from p-type to n-type charge transport characteristics.[10] Similarly, nitrogen onium salts derived from N-doped PAHs exhibit intriguing optoelectronic properties and self-assembly behavior.[11] A notable example is the *N*-methylated pyridinium salts of N-doped PAHs, which have demonstrated

[a]*Research Center for Free Radical Chemistry, State Key Laboratory of Applied Organic Chemistry, Lanzhou University, Tianshui Southern Road 222, Lanzhou, Gansu Province, China. E-mail: shaoxf@lzu.edu.cn*

[b]*College of Chemistry and Chemical Engineering, College of Biomedical Sciences, Inner Mongolia Key Laboratory of Synthesis and Application of Organic Functional Molecules, Inner Mongolia University, Hohhot 010021, P. R. China. E-mail: wangjg@iccas.ac.cn*

† Electronic supplementary information (ESI) available. CCDC 2423790–2423792. For ESI and crystallographic data in CIF or other electronic format see DOI: https://doi.org/10.1039/d5sc02061a

‡ These authors contributed equally: Yao Ma, Dongxu Li, Xin Chen.

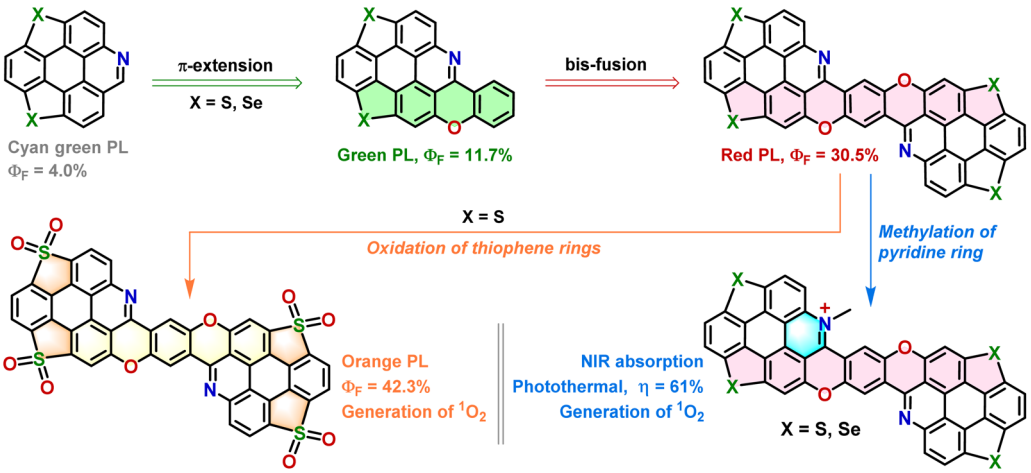

Scheme 1 The molecular design principles underlying this work.

broad applicability in fluorescent dyes, cellular imaging, and phototheranostic applications.[12]

Given the growing demand for high-performance organic materials, rational molecular design strategies involving heteroatom doping and valence state manipulation of PAHs offer an exciting platform for tailoring optoelectronic properties. Herein, we report the design, synthesis, and optical properties of a series of multi-heteroatom-doped PAHs. Our molecular engineering approach integrates three key strategies: (i) multi-element heteroatom doping, (ii) π-conjugation extension, and (iii) main-group element valence state modulation.

We have synthesized a kind of hetero-PAHs co-doped with nitrogen and chalcogen,[7c] which display cyan green fluorescence with quantum yield (Φ_F) of 4.0% (Scheme 1). Expanding the π-system plays a pivotal role in tuning absorption and emission properties. By fusing a benzopyran unit onto the periphery of a PAH scaffold, we introduce an additional oxygen dopant, achieving a bathochromic shift in absorption and emission with an enhanced Φ_F of 11.7%. Further π-extension through bis-fusion results in red fluorescence with a significantly improved Φ_F of 30.5%. Finally, the manipulation of valence states of heteroatom dopants is conducted, resulting distinct modulation on the electronic structures. Oxidation of thiophene rings to thiophene *S*,*S*-dioxides enhances the Φ_F to 42.3% and enables efficient $^1O_2$ generation. Meanwhile, pyridinium-functionalized hetero-PAHs exhibit strong NIR absorption, leading to high photothermal conversion efficiency (up to 61%) at the molecular level. Notably, selenium-doped derivatives outperform their sulfur analogs, highlighting the heavy-atom effect in triplet-state modulation. This work provides a facile synthetic approach for constructing multi-heteroatom-doped PAHs with tunable electronic structures and promising potential in phototheranostics.

Results and discussion

Synthesis of N, O, and S/Se co-doped hetero-PAHs

Developing efficient synthetic strategies for hetero-PAHs co-doped with nitrogen (N) and chalcogen atoms (O, S, and Se) is challenging. Herein, we report a scalable and systematic approach toward such kind of hetero-PAHs. To achieve the efficient synthesis of them, it is advantageous to begin with starting materials that are already doped with one of these heteroatoms. In this study, compounds **1a**/**1b**, which feature sulfur (S) or selenium (Se) in their π-scaffolds, were selected as the precursors. These compounds are particularly suitable due to their scalable synthesis as reported in our previous work.[7c] Using a combination of acid-catalyzed Pictet–Spengler (P–S) reactions[13] and thermally induced *ipso*-substitutions,[7b] a series of hetero-PAHs co-doped with N, O, and S/Se were synthesized efficiently (Scheme 2).

The synthesis began with nitration of **1a**/**1b** using *tert*-butyl nitrite (TBN) at room temperature (RT), followed by reduction with Zn/AcOH to yield intermediates **2a**/**2b** in overall yields of 80% and 72%, respectively. The subsequent P–S reaction with benzaldehyde, catalyzed by trifluoroacetic acid (TFA), afforded **3a**/**3b** in yields of 71% and 73%, respectively. Similarly, reacting **2a**/**2b** with salicylaldehyde provided **4a**/**4b** in isolated yields of 60% and 75%. To construct the final framework of the desired hetero-PAHs, thermally induced intramolecular *ipso*-substitution of **4a**/**4b** was performed by heating at 185 °C under vacuum for 12 hours, yielding **5a**/**5b** in isolated yields of 74%/92%. Furthermore, the P–S reaction of **2a**/**2b** with 2,5-dihydroxy-1,4-benzenedicarboxaldehyde enabled a two-fold ring-cyclization, giving **6a**/**6b** in yields of 51%/66%. The intermediates **6a**/**6b** underwent a two-fold thermally induced *ipso*-substitution to afford **7a**/**7b** in yields of 76%/81%. As a result, the hetero-PAHs **5a**/**5b** and **7a**/**7b**, co-doped with N, O, and S/Se, were successfully synthesized. This method demonstrates a robust and scalable pathway for synthesizing hetero-PAHs with tailored doping profiles. Remarkably, the structure of **7a**/**7b** features a novel subunit that can be conceptualized as a hetero-heptacene framework (painted with red background in Scheme 2), which is composed of alternating chalcogenole, pyran, and pyridine moieties. Needless to say, this is the first construction of such kind of hetero-acenes.

Manipulation of the valence states of heteroatom dopants

To further tailor the optoelectronic properties of the synthesized hetero-PAHs, we explored the valence state manipulation

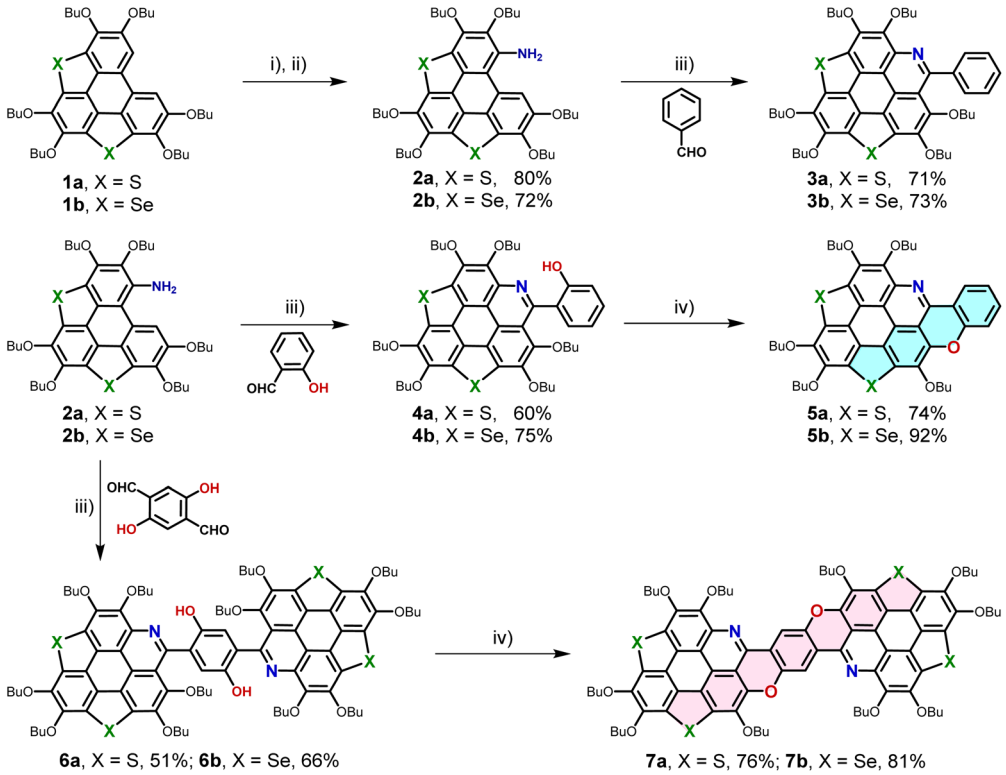

Scheme 2 Synthesis of hetero-PAHs **5a**/**5b** and **7a**/**7b**. Reagents and conditions: (i) TBN (2.0 equiv.), CH_2Cl_2, RT, 4 h; (ii) Zn powder (7.0 equiv.), AcOH (2.0 equiv.), C_2H_5OH-THF (v/v = 2 : 5), 90 °C, 6 h; (iii) TFA, 120 °C, 12 h; (iv) 185 °C for 12 h under vacuum.

of the heteroatom dopants. Thiophene *S*,*S*-dioxides are well-documented for their excellent photoluminescence (PL) properties[9] and n-type charge transport behavior,[10a,d] making their incorporation a promising strategy for enhancing material performance. To this end, the thiophene moieties in **5a** and **7a** were selectively oxidized to thiophene *S*,*S*-dioxides under optimized conditions (Scheme 3). The oxidation of **5a** using hydrogen peroxide (H_2O_2) proceeded efficiently, yielding compound **8a** with a 60% isolated yield.[14] However, the oxidation of **7a** with H_2O_2 resulted in complex mixtures that were hard to isolate by column chromatography. This limitation was overcome by employing *meta*-chloroperoxybenzoic acid (*m*CPBA) as the oxidant, which selectively oxidized the thiophene units in **7a** to their corresponding *S*,*S*-dioxides, affording **9a** in a yield of 40%.[15] These results underscore the critical role of oxidant choice in controlling the reaction outcome.

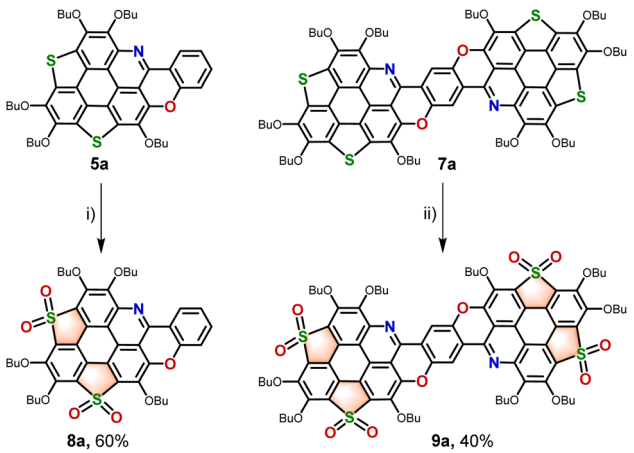

Scheme 3 Synthesis of **8a** and **9a**. Reagents and conditions: (i) H_2O_2 (30% aqueous), $CHCl_3$–AcOH (v/v = 1 : 1), 60 °C, 6 h; (ii) *m*CPBA (10.0 equiv.), $CHCl_3$, 60 °C, 12 h.

Additionally, the electronic structure of pyridine-containing hetero-PAHs will be altered by transforming the pyridine moieties into pyridinium salts.[12] Hence, the pyridine moieties on **5a**/**5b** and **7a**/**7b** were transformed into the pyridinium salts as shown in Scheme 4. Methylation of the pyridine rings in **5a**/**5b** and **7a**/**7b** using methyl trifluoromethanesulfonate (MeOTf) at 120 °C afforded pyridinium salts **10a**/**10b** (isolated yields, 62%/62%) and **11a**/**11b** (isolated yields, 60%/66%). This transformation introduced a strong electron-withdrawing effect, significantly lowering the electron density across the PAH framework and further tuning their electronic properties. The integration of scalable starting materials, controlled doping, and post-synthetic valence state modulation demonstrates a versatile approach for tailoring the electronic structures and optoelectronic properties of PAHs.

Molecular structures

To gain insight into the effects of π-system extension, heteroatom doping, and the valence state of dopants on molecular conformations, the structures of these hetero-PAHs were

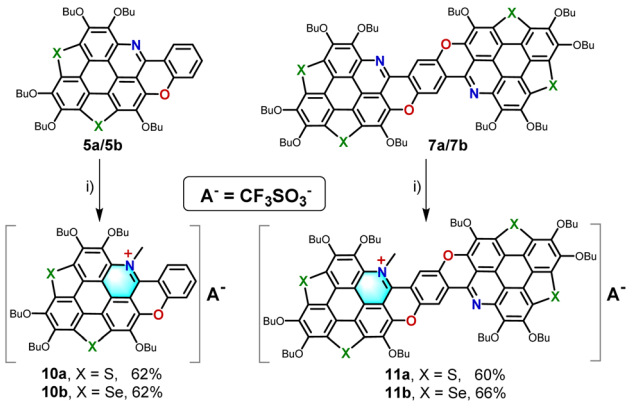

Scheme 4 Synthesis of **10a**/**10b** and **11a**/**11b**. Reagents and conditions: (i) MeOTf (3.0 equiv.), toluene, 120 °C, 12 h.

analyzed by theoretical calculations and single-crystal X-ray diffraction.

The molecular structures of compounds **3a**/**3b**, **5a**/**5b**, and **7a**/**7b**–**11a**/**11b** were optimized at the B3LYP/Def2-SVP level of theory, with *n*-butyl groups replaced by methyl groups, yielding **3a′**/**3b′**, **5a′**/**5b′**, and **7a′**/**7b′**–**11a′**/**11b′**. The optimized structures of hetero-PAHs co-doped with N, O, and S are shown in Fig. 1, while those doped with N, O, and Se are presented in Fig. S39–S43.† Compound **3a′** adopts a bowl-shaped conformation with a bowl-depth of 0.32 Å (Fig. 1a). However, upon fusing a pyran moiety to the core structure, as in **5a′**, the molecule has a nearly planar π-framework (Fig. 1b), suggesting that the introduction of the pyran moiety induces a flattening of the curved π-system. Oxidation of the thiophene moieties in **5a′** to thiophene *S*,*S*-dioxides further flattens the structure, resulting in a completely planar π-scaffold of **8a′** (Fig. 1c). In contrast, methylation of the pyridine ring in **5a′** leads to a shift from a planar structure to a bowl-shaped conformation in **10a′** (bowl-depth, 0.34 Å) as shown in Fig. 1d. Moreover, extension of the π-system from **5a′** to **7a′** changes the molecular conformation from planar to S-shaped, with bowl-depths of 0.41 Å and 0.31 Å for the two segments of **7a′** respectively (Fig. 1e). It is also found that altering the valence states of heteroatom dopants in **7a′** causes significant changes in molecular geometry. For instance, compound **9a′** takes a nearly planar conformation (Fig. 1f), while **11a′** possesses a boat-like conformation with bowl-depths of 0.43 Å and 0.36 Å for the two segments (Fig. 1g).

The results demonstrate that molecular conformation of these hetero-PAHs is highly influenced by the extension of the π-system, the nature of heteroatom doping, and the valence state of the dopants. The valence state modulation of heteroatoms in particular plays a crucial role in controlling molecular geometry, from curved to planar or even boat-like conformations. These insights are crucial for the rational design of molecular materials where control over the conjugation and structure can lead to tunable electronic properties.

Fortunately, we have obtained the single crystals of **9a**, **10a**, and **10b** which were suitable for X-ray single-crystal diffraction analysis. Red needle-like crystals of **9a** were grown by slow evaporation of a chlorobenzene solution at RT, while dark blue needle-like single crystals of **10a** and **10b** were harvested from a mixed solvent system of CH_2Cl_2 and CH_3OH (v/v = 1 : 1). Herein, the crystal structures of **9a** and **10a** will be reported. The crystal structure of **10b** is similar to that of **10a** and is shown in Fig. S5.†

Compound **9a** crystallizes in the $P\bar{1}$ space group. The crystal contains two distinct molecules (**A** and **B**), with molecule **A** and half of molecule **B** being crystallographically unique. Both molecules exhibit similar geometries, with the structure of molecule **A** depicted in Fig. 2a and b. The C=C bond lengths in the triphenylene moiety of **A** are consistent with those observed

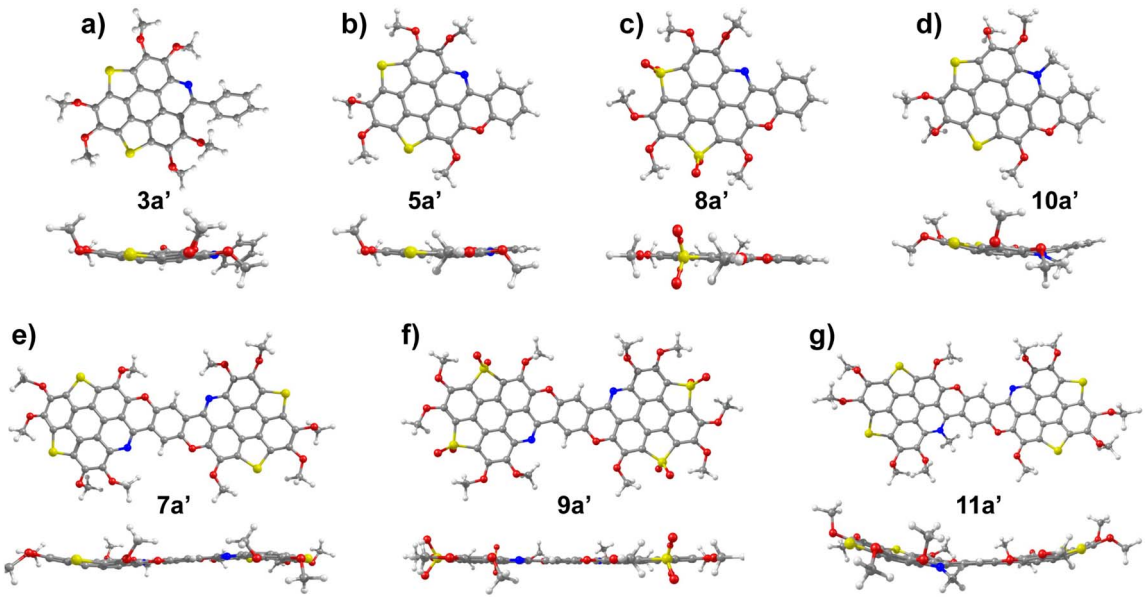

Fig. 1 Optimized molecular structures of (a) **3a′**, (b) **5a′**, (c) **8a′**, (d) **10a′**, (e) **7a′**, (f) **9a′**, and (g) **11a′**.

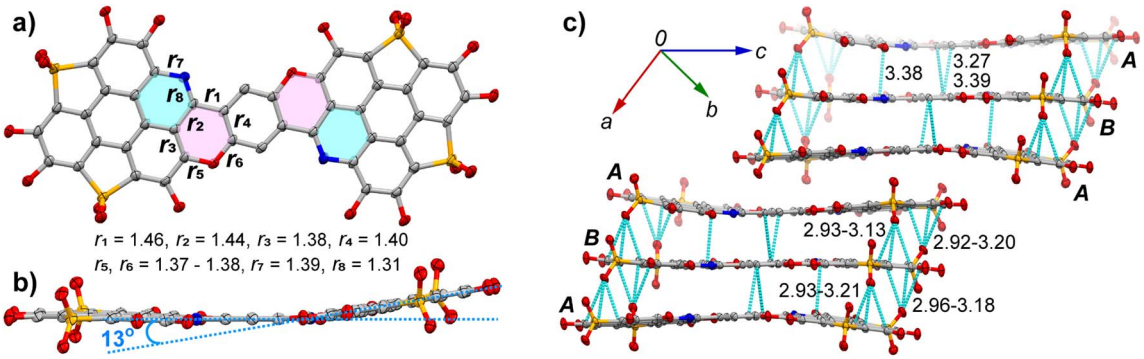

Fig. 2 Crystal structure of **9a** with *n*-butyl groups and hydrogen atoms omitted for clarity. (a) Top view of molecule **A** with selected bond lengths shown in unit of Å; (b) side view of **A**, showing the dihedral angle between the two planar subunits (cyan dashed lines); (c) packing structure with intermolecular short contacts shown in green dashed lines. The C, N, O, and S atoms are colored in grey, blue, red, and orange, respectively.

in trichalcogenasumanenes.[6d] However, the C=C bonds within the pyran ring, highlighted in red in Fig. 2a, show notable bond length variation: bonds r_1 (1.46 Å) and r_2 (1.44 Å) are clearly longer than r_3 (1.38 Å) and r_4 (1.40 Å). The two C–O bonds (r_5 and r_6) in the pyran ring are nearly identical in length, measuring 1.37–1.38 Å. In contrast, the two C–N bonds in the pyridine ring (highlighted in blue) differ significantly, with r_7 = 1.39 Å and r_8 = 1.31 Å. Molecule **A** adopts a curved π-framework (Fig. 2b), with a dihedral angle of 13° between the mean planes of the two conjugated subunits (cyan dashed lines). In the crystal, molecules **A** and **B** aggregate in a columnar arrangement (Fig. 2c). Within the stacking columns, two **A** molecules and one **B** molecule form a trimer through multiple intermolecular C···C contacts (3.27–3.39 Å) between their π-frameworks, as indicated by green dashed lines. Additionally, C···O interactions (2.92–3.21 Å) are observed between the carbon π-framework and oxygen atoms on the thiophene *S*,*S*-dioxide units. Neighboring trimers are further connected by van der Waals interactions between their butoxyl chains.

Compound **10a** adopts the $P2_1/c$ space group with the asymmetric unit contains one molecule. The crystal structure of **10a** is presented in Fig. 3. Similar to **9a**, bond length variation is observed in the pyran ring, where r_1 (1.45 Å) is longer than r_2 (1.42 Å), r_3 (1.41 Å), and r_4 (1.41 Å) as shown in Fig. 3a. In comparison with **9a**, the formation of a pyridinium salt in **10a** gives rise to the elongation of the C–N bonds in the pyridine ring, with r_7 = 1.43 Å and r_8 = 1.36 Å. The π-conjugated skeleton of **10a** is nearly planar, with an average deviation of 0.023 Å (Fig. 3b). However, steric hindrance from the methyl group on the pyridinium salt causes deviations from the π-conjugated plane, particularly for the nitrogen atom (0.245 Å), C_{24} (0.162 Å), and C_{25} (0.160 Å). Moreover, the methyl group on the pyridinium is distinctly displaced from the π-conjugated plane, with a torsion angle of 26° between the methyl group and the terminal benzene. In the crystal, **10a** adopts a columnar arrangement (Fig. 3c), where **10a** molecules are dimerized in a head-to-tail manner due to dipole–dipole interactions. Within a dimer, there are four C···C contacts (3.36–3.37 Å) between the π-frameworks of two molecules. Similar as that observed in **9a**, the neighboring dimers of **10a** are connected by van der Waals interactions between their butoxyl chains.

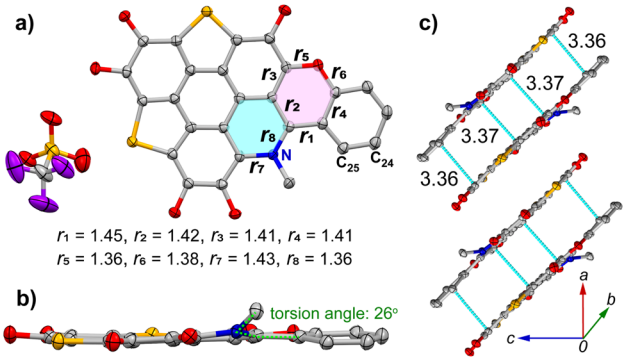

Fig. 3 Crystal structure of **10a** with *n*-butyl groups and hydrogen atoms omitted for clarity. (a) Top view of molecule with the selected bond lengths in unit of Å; (b) side view with torsion angle shown; (c) packing structure with intermolecular short contacts shown in green dashed lines. The C, N, O, F, and S atoms are colored in grey, blue, red, purple, and orange, respectively.

It is worth of noting that the optimized molecular structures of **9a**/**10a** are different from those observed in their crystal structures. The key reason is attributed to the packing effect on the molecular conformation as has been documented in the early reports.[14b,16] For instance, the strong interactions between the carbon π-framework and oxygen atoms on the thiophene *S*,*S*-dioxide units in **9a** result in the deformation of molecular conformation.

Electronic structures

The electronic structures of the hetero-PAHs under investigation were analyzed through density functional theory (DFT) calculations. The frontier molecular orbitals (FMOs) of the hetero-PAHs were computed at the B3LYP/Def2-TZVP level of theory, based on the optimized structures of **3a′**/**3b′**, **5a′**/**5b′**, and **7a′**/**7b′**–**11a′**/**11b′**. The calculated HOMO, LUMO, and energy levels for compounds **3a′**, **5a′**, **7a′**, **9a′**, and **11a′** are presented in Fig. 4. The N, O, and Se co-doped hetero-PAHs exhibit similar features as presented in Fig. S39–S43.†

In the case of **3a′**, the HOMO and LUMO are delocalized over the π-conjugated core, which consists of a triphenylene unit

and two thiophene rings. Notably, the pyridine ring and terminal benzene ring contribute largely to the LUMO. For **5a′**, the LUMO retains a similar distribution as in **3a′**, but the HOMO extends across the π-conjugated core and the benzopyran moiety. As a result, the LUMO levels of **5a′** (−1.89 eV) and **3a′** (−1.96 eV) are comparable, but the HOMO level of **5a′** (−5.09 eV) is higher than that of **3a′** (−5.29 eV). This shift in energy of FMOs reflects the stabilization effect from the fusion of benzopyran moiety, which is further confirmed by the extension of π-framework from **5a′** to **7a′**. The delocalization of π-electrons is markedly enhanced in **7a′**, as evidenced by the HOMO and LUMO distributions. While the HOMO level of **7a′** (−5.05 eV) remains almost identical to that of **5a′** (−5.09 eV), the LUMO level of **7a′** (−2.41 eV) is distinctly lower than that of **5a′** (−1.89 eV). Consequently, the HOMO–LUMO gap (E_g) narrows in the order: **3a′** (3.33 eV) > **5a′** (3.20 eV) > **7a′** (2.64 eV).

Upon oxidation of the thiophene rings in **7a′** to thiophene *S*,*S*-dioxides, as in **9a′**, the thiophene *S*,*S*-dioxides contribute minimally to the HOMO coefficient, as observed in both **9a′** and **8a′** (Fig. S35–S36†). Both the HOMO (−3.19 eV) and LUMO (−5.84 eV) energy levels of **9a′** decrease markedly as compared to **7a′**, which is attributed to the transformation of electron-rich thiophene rings into electron-deficient thiophene *S*,*S*-dioxides. Despite these shifts, the E_g-value of **9a′** (2.65 eV) is comparable to that of **7a′**.

Finally, methylation of the pyridine ring in **7a′** results in a significant change in both the HOMO and LUMO coefficients and their respective energy levels. In **11a′**, the HOMO and LUMO are localized on segments without and with the methylation, respectively. This spatial separation of HOMO and LUMO suggests the potential for intramolecular charge-transfer (ICT) transitions. Compared to **7a′** and **9a′**, the HOMO (−5.56 eV) and LUMO (−7.12 eV) energy levels of **11a′** are significantly lowered, and the E_g-value (1.57 eV) of **11a′** is much narrower than those of **7a′** and **9a′**.

The computational investigations reveal that the extension of the π-conjugation leads to enhanced electron delocalization and narrowing of HOMO–LUMO gap. Furthermore, the modifications on the valence states of dopants, such as oxidation and methylation, introduce significant changes to the electronic properties. This systematic control over the electronic structure highlights the tunability of these materials.

Photophysical properties

The photophysical properties of the present hetero-PAHs were systematically evaluated using UV-vis absorption and emission spectroscopy. As representative examples, Fig. 5 illustrates the UV-vis absorption and emission spectra for the N, O, and S co-doped PAHs co-doped **3a**, **5a**, **7a**, **8a**, and **9a** in the $CHCl_3$ solution ($c = 1 \times 10^{-5}$ mol L^{-1}) measured at RT.

Compound **3a** exhibits three distinct absorption peaks at 299 nm, 328 nm, and 341 nm, alongside a broad absorption band spanning 365–470 nm (Fig. 5a). Upon extending the π-system by fusing a benzopyran moiety onto **3a**, as seen in compound **5a**, the absorption spectrum shifts bathochromically. Specifically, **5a** displays a sharp absorption peak at 309 nm and a broader band at 390–500 nm, indicating the influence of π-system extension on the electronic structure. A further extension of π-system in **7a** leads to a significantly broadened low-energy absorption band, which shifts to 430–600 nm. These trends are consistent with the calculated energy gaps (E_g) for **3a**, **5a**, and **7a**.

Theoretical simulations using time-dependent DFT (TD-DFT) at the TD-ωB97X/Def2-SVP/IEFPCM($CHCl_3$) level (Fig. S54–S65 and Tables S7–S18†) provide further insight into these trends. For **3a**, the lowest energy absorption band is attributed to the $S_0 \rightarrow S_2$ transition with an excitation energy (ΔE) of 3.61 eV and an oscillator strength (f) of 0.2673. This excitation primarily involves the HOMO → LUMO transition

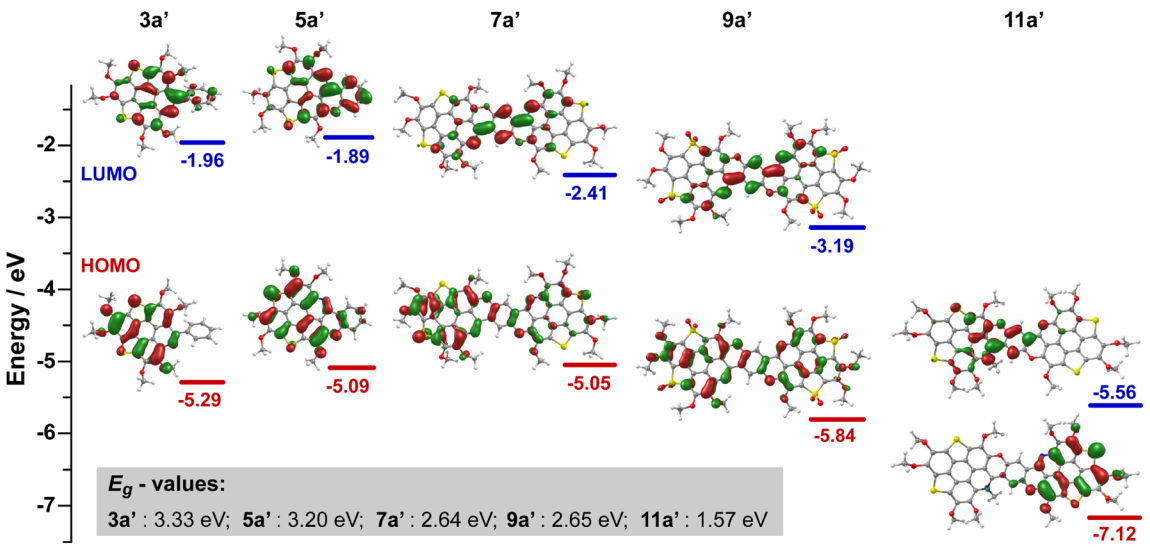

Fig. 4 Calculated frontier molecular orbitals (FMOs) and energy levels of 3a′, 5a′, 7a′, 9a′, and 11a′.

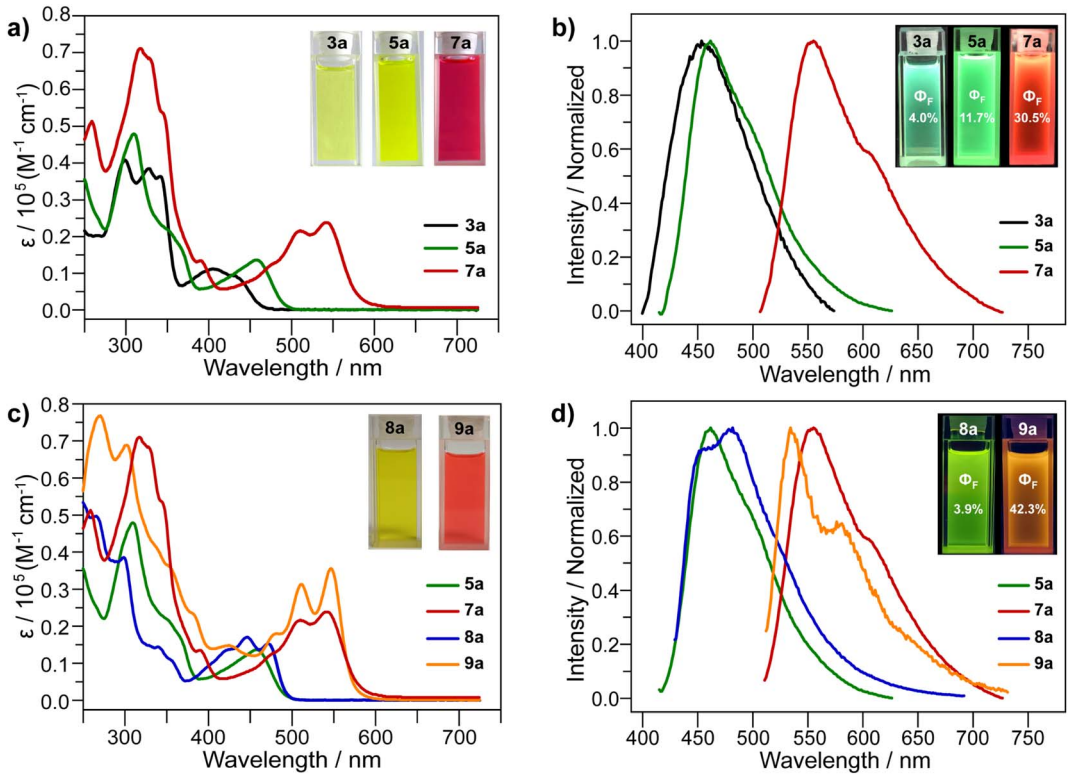

Fig. 5 Absorption and emission spectra of N, O, and S co-doped hetero-PAHs measured in $CHCl_3$ ($c = 1 \times 10^{-5}$ mol L^{-1}): (a) UV-vis absorption and (b) emission spectra for **3a**, **5a**, and **7a**; (c) UV-vis absorption and (d) emission spectra of **5a**, **7a**, **8a**, and **9a**.

(66.5% contribution). For **5a** and **7a**, the lowest energy absorption bands correspond to the $S_0 \rightarrow S_1$ transition, with ΔE values of 3.28 eV ($f = 0.3963$) and 2.96 eV ($f = 1.0927$), respectively. The excitations in both cases predominantly arise from the HOMO → LUMO transition (>79.0% contribution).

In terms of emission properties, **3a** exhibits green fluorescence with a maximum emission (λ_{em}) at 496 nm and Φ_F of 4.0% (Fig. 5b). Upon modification on molecular structures, **5a** displays a slightly red-shifted emission ($\lambda_{em} = 503$ nm) and an improved Φ_F of 11.7%. In contrast, **7a** shows a distinct red-shift in its fluorescence with λ_{em} at 585 nm and a higher Φ_F of 30.5%.

The oxidation of the thiophene rings in **5a** and **7a** to thiophene *S*,*S*-dioxides, resulting in compounds **8a** and **9a**, induces further modulation of the photophysical properties. The absorption spectrum of **8a** is slightly red-shifted compared to **5a** (Fig. 5c), while **9a** exhibits a slight blue-shift relative to **7a**. TD-DFT simulations reveal that the lowest energy absorption bands of both **8a** and **9a** are attributed to the $S_0 \rightarrow S_1$ transition, with ΔE values of 3.28 eV ($f = 0.5221$) and 2.97 eV ($f = 1.1726$), respectively (Fig. S60, S61 and Tables S13, S14†). These transitions predominantly arise from the HOMO → LUMO transition (>77.9% contribution). Notably, the oscillator strengths for these excitations are larger than those of **5a** and **7a**, resulting in stronger low energy absorption features for **8a** and **9a**. Fluorescence measurements show that **8a** exhibits green emission ($\lambda_{em} = 520$ nm), red-shifted by approximately 17 nm compared to **5a** (Fig. 5d), while **9a** displays blue-shifted emission ($\lambda_{em} = 565$ nm) compared to **7a**. The Φ_F of **9a** is much enhanced to 42.3%, surpassing that of **7a**. In contrast, the Φ_F of **8a** is reduced to 3.9%, which is lower than that of **5a**.

Further chemical modification through methylation of the pyridine rings on **5a** and **7a** to form compounds **10a** and **11a** leads to substantial changes in the absorption spectra. As shown in Fig. 6, **10a** exhibits a broad absorption band between 410–670 nm, with the absorption maximum red-shifted by approximately 106 nm compared to **5a**. For **11a**, the low-energy absorption extends into the near-infrared (NIR) region, say, 600–860 nm. TD-DFT simulations indicate that the lowest energy absorption bands for **10a** and **11a** correspond to the $S_0 \rightarrow S_1$ transition (Fig. S62–S64 and Tables S15–S17†). For **10a**, this excitation is dominated by the HOMO → LUMO transition (91.0% contribution), with $\Delta E = 2.62$ eV and $f = 0.2791$. For **11a**, the $S_0 \rightarrow S_1$ excitation arises from a combination of the HOMO → LUMO and HOMO-2 → LUMO transitions, with contributions of 58.3% and 27.2%, respectively. The calculated excitation energy for **11a** is 2.40 eV, and the oscillator strength is 0.8097.

These results indicate that photophysical properties of hetero-PAHs can be effectively tuned through structural modifications, particularly the extension or alteration of the π-system and functional group modifications such as oxidation and methylation, which can significantly impact absorption, emission, and fluorescence quantum yield.

The optical properties of compounds **7a**/**7b** and **11a**/**11b** display notable tunability under acidic conditions. Representative examples are shown in Fig. 7, which illustrates the

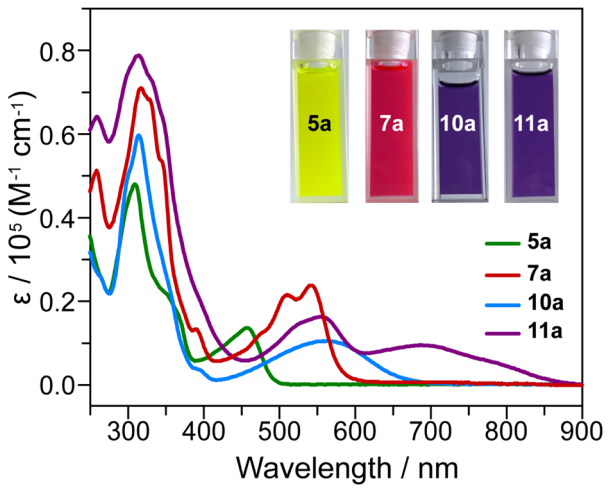

Fig. 6 UV-vis-NIR absorption spectra of **5a**, **7a**, **10a** and **11a** in $CHCl_3$ ($c = 1 \times 10^{-5}$ mol L^{-1}).

spectroscopic behavior of **7a** and **11a** upon treatment with trifluoroacetic acid (TFA), alongside theoretical simulation results. Compounds **7b** and **11b** exhibit similar trends, as shown in Fig. S11, S12 and S48–S51.†

As shown in Fig. 7a, gradual addition of TFA to a $CHCl_3$ solution of **7a** ($c = 1 \times 10^{-5}$ mol L^{-1}) leads to a decrease in the absorption band at 430–600 nm and the emergence of a new band spanning 450–850 nm, with a maximum at 663 nm. Concurrently, the solution color transitions from red to magenta (TFA, 100 eq.), then to blue (TFA, 1000 eq.), and finally to dark green (TFA, 3000 eq.). Notably, the UV-vis-NIR absorption spectrum of **7a** treated with 200 equivalents of TFA closely resembles that of pure **11a** in $CHCl_3$, suggesting structural and electronic convergence upon protonation. In addition, the fluorescence of **7a** is quenched upon TFA addition, as shown in Fig. 7b.

Upon titration of **11a** with TFA (Fig. 7c), the original absorption band at 425–610 nm disappears, and a new band appears between 460–850 nm, with a λ_{max} at 680 nm. Under conditions of excess TFA, both **7a** and **11a** converge to similar UV-vis-NIR absorption profiles, indicating stepwise protonation of the two pyridine rings in **7a**.

Theoretical calculations support the notion that protonation of **7a** is electronically analogous to methylation. As illustrated in Fig. 7d, the HOMO (−7.02 eV) and LUMO (−5.48 eV) energy levels, along with the energy gap (E_g = 1.54 eV) of the monoprotonated species **7a′[H⁺]**, closely match those of **11a′**. Furthermore, the doubly protonated species **7a′[H⁺]₂** displays electronic characteristics similar to the further protonated form of **11a′**, with both showing decreased HOMO and LUMO energy levels and a slightly altered E_g. The doubly methylated **7a′**

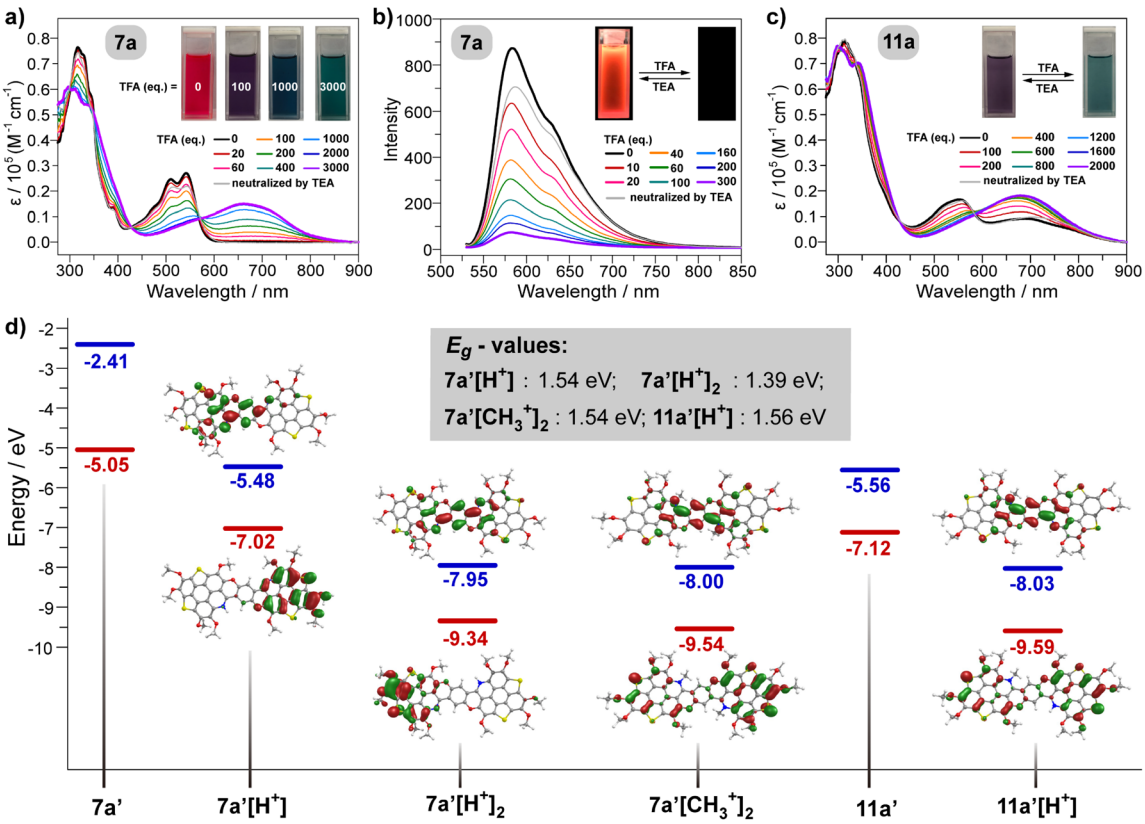

Fig. 7 (a) UV-vis and (b) emission spectra of **7a** upon titration with TFA; (c) UV-vis-NIR of **11a** upon titration with TFA; (d) calculated frontier molecular orbitals (FMOs) and energy levels of **7a′**, **7a′[H⁺]**, **7a′[H⁺]₂**, **11a′**, **11a′[H⁺]** and **7a′[CH_3^+]₂**. Measurement conditions: 20 °C, $CHCl_3$ solution with $c = 1 \times 10^{-5}$ mol L^{-1}.

$[CH_3^+]_2$ exhibits HOMO (−9.54 eV), LUMO (−8.00 eV), and E_g (1.54 eV) values comparable to those of the doubly protonated **7a′**$[H^+]_2$, further supporting the electronic analogy between methylation and protonation.

Generation of singlet oxygen ($^1O_2$)

Phototheranostics, composed of photodynamic therapy (PDT) and photothermal therapy (PTT), have garnered significant attention due to their noninvasive nature, high precision, and minimal side effects on healthy tissues.[17] PDT is an effective tumor treatment strategy that utilizes photosensitizers (PSs) to generate reactive oxygen species (ROS), particularly $^1O_2$, upon light irradiation, thereby inducing cellular apoptosis.[18] The development of organic PDT materials has focused on optimizing photophysical properties, including extending absorption spectra to longer wavelength to enhance tissue penetration and increasing Φ_F. A key strategy involves designing conjugated polymers or small organic molecules with large π-systems and incorporating heavy atoms to facilitate intersystem crossing (ISC) and improve ROS generation efficiency.[8,19] Additionally, push–pull organic frameworks, featuring integrated electron-donating and electron-accepting groups, have demonstrated great potential for enhancing PDT performance by fine-tuning absorption properties and increasing $^1O_2$ production.

In this study, compounds **7a**/**7b**, **9a**, and **11a**/**11b** exhibit potential as PSs for $^1O_2$ generation, owing to their large π-systems and the presence of heavy chalcogen dopants (S, Se). The ability of these compounds to generate $^1O_2$ was evaluated using 1,3-diphenylisobenzofuran (DPBF) as an oxidative probe, which undergoes a ring-opening reaction in the presence of $^1O_2$ (Fig. 8a), leading to a decrease in its absorption at ∼415 nm.[20] A control experiment showed that, in the absence of PSs, DPBF's absorption remained unchanged under light irradiation (660 nm) for 10 minutes (Fig. S19†). However, upon the addition of **7a**/**7b**, **9a**, and **11a**/**11b** (10 μM), the DPBF absorption at 415 nm significantly decreased, confirming efficient $^1O_2$ production. Time-dependent absorption spectra for DPBF in the presence of representative PSs (**9a**, **11a**, and **11b**) are shown in Fig. 8b–d, while those for **7a**/**7b** are provided in Fig. S20 and S21.†

Using **7a** as a PS, the DPBF absorbance at 415 nm declined to 15% of its original value after 15 minutes of irradiation (Fig. S20†). In contrast, **9a** exhibited more efficient $^1O_2$ production, completely quenching DPBF within 10 minutes (Fig. 8b). Similarly, **11a** reduced the DPBF absorbance to 20% within 10 minutes (Fig. 8c). These results indicate that the manipulation of the valence states of heteroatom dopants shows significant influence on the efficiency of $^1O_2$ generation. A notable approach to enhancing $^1O_2$ generation is replacing sulfur with selenium, as demonstrated by the superior performance of **7b** and **11b**. The DPBF absorbance at 415 nm dropped rapidly, almost disappearing after 5 minutes with **7b** as the PS (Fig. S21†). Remarkably, with **11b**, complete degradation of DPBF was observed within just 2 minutes (Fig. 8d).

The decay rates of DPBF absorption (Fig. 8e) indicate the order of $^1O_2$ generation efficiency: **7a** < **11a** < **9a** < **7b** < **11b**. The superior performance of Se-doped PSs (**7b** and **11b**) over S-doped analogs (**7a**, **9a**, and **11a**) is attributed to the heavy-atom effect, which enhances ISC and stabilizes the triplet state.[21] Furthermore, the higher photosensitizing ability of **11b** compared to **7b** is primarily ascribed to its smaller singlet-triplet energy gap ($\Delta E_{S_1-T_1}$). TD-DFT calculations reveal that $\Delta E_{S_1-T_1}$ for **11b** is 0.20 eV (Fig. 8f), significantly lower than that of

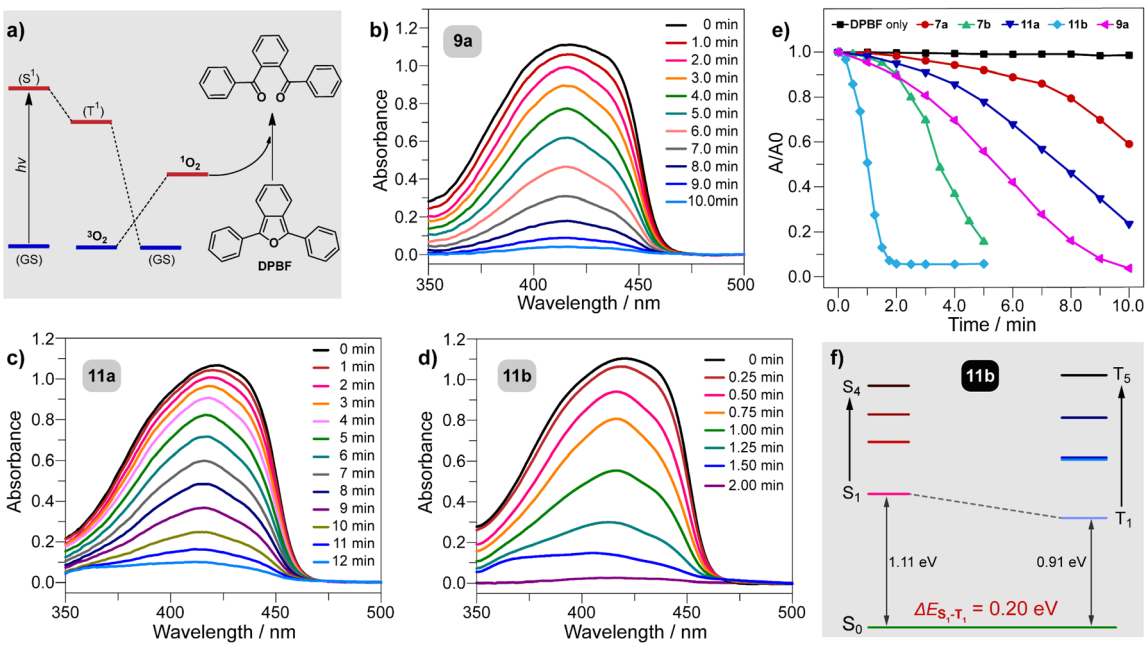

Fig. 8 (a) Chemical process for the ring-opening reaction of DPBF in the presence of $^1O_2$ generated by PSs; time-dependent absorption spectra of DPBF (in CH_2Cl_2, $c = 1 \times 10^{-4}$ mol L^{-1}) upon irradiation at 660 nm (2.5 W cm^{-2}) in the presence of (b) **9a**, (c) **11a**, (d) **11b**; (e) decay rate of DPBF absorbance at 415 nm with different PSs; (f) energy level diagram of singlet and triplet excited states of **11b**.

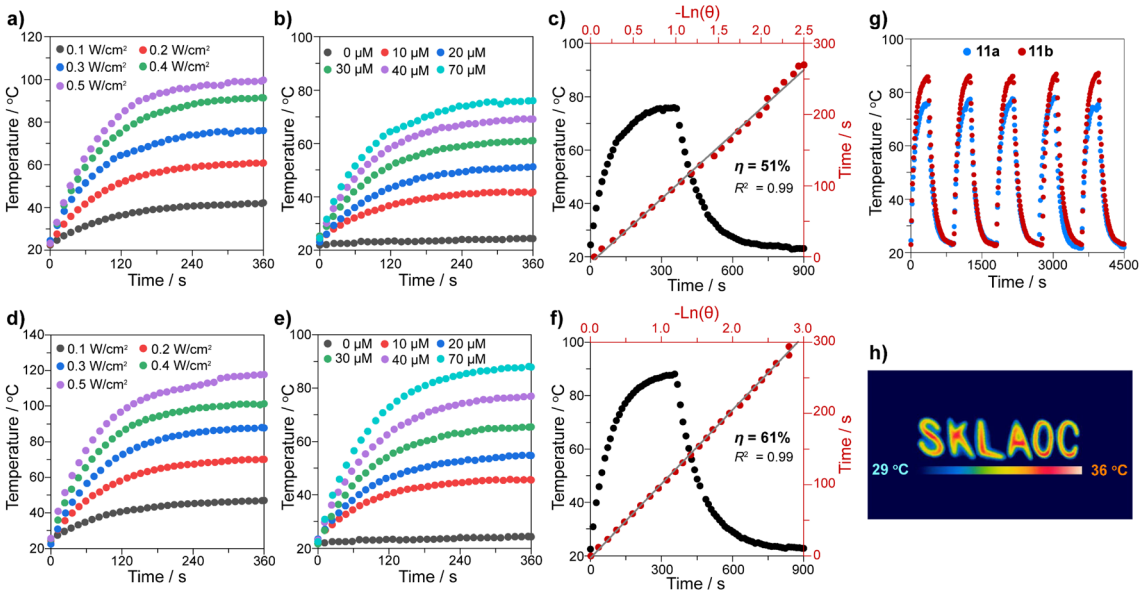

Fig. 9 Photothermal properties of **11a**/**11b** in *o*-dichlorobenzene solution under 660 nm laser irradiation: (a) power-dependent (70 μM) and (b) concentration-dependent (0.3 W cm^{-2}) temperature, and (c) temperature increasing/decreasing curve (70 μM, 0.3 W cm^{-2}) and calculation of η (θ: temperature driving force) of **11a**; (d) power-dependent (70 μM) and (e) concentration-dependent (0.3 W cm^{-2}), and (f) temperature increasing/decreasing curve (70 μM, 0.3 W cm^{-2}) and calculation of η of **11b**; (g) photothermal stabilities of **11a**/**11b** during 5 cycles of heating-cooling (70 μM, 0.3 W cm^{-2}); (h) photothermal images of **11a** (irradiation for 60 s, 0.5 W cm^{-2}).

7b (0.52 eV), thereby facilitating more efficient $^1O_2$ generation. Additionally, the higher fluorescence quantum yield (Φ_F) of **9a** (42.3%) compared to **7a** (Φ_F = 30.5%) further accounts for its enhanced PDT performance.[22]

Photothermal performance

PTT employs light-absorbing materials to convert light energy into heat, effectively inducing tumor cell apoptosis by localized hyperthermia.[23] Organic PSs with strong near-infrared (NIR) absorption (600–1000 nm) are highly promising candidates for PTT applications.[2g,24] In this study, compounds **11a**/**11b** exhibit broad absorption bands spanning 600–860 nm, making them well-suited for PTT. Their photothermal characteristics were thoroughly investigated under 660 nm laser irradiation.

The photothermal properties of **11a**/**11b** were evaluated by monitoring temperature changes in their *o*-dichlorobenzene solutions using an infrared thermal camera. As shown in Fig. 9a, the temperature of **11a** solution steadily increases upon irradiation, reaching a plateau within 6 minutes. The maximum stable temperature (T_{max}) increases with power density and reaches 100 °C at 0.5 W cm^{-2}. T_{max} also exhibits concentration dependence, rising from 42 °C to 79 °C as the concentration of **11a** increases from 10 μM to 70 μM (Fig. 9b). According to the reported method,[25] the photothermal conversion efficiency (η) of **11a** was calculated to be 51% based on a heating-cooling cycle experiment (Fig. 9c).

Compared to **11a**, **11b** demonstrated similar power- and concentration-dependent trends but exhibited superior photothermal performance. Under identical irradiation conditions, the T_{max} of **11b** reached 118 °C at 0.5 W cm^{-2} (Fig. 9d). As the concentration of **11b** increases from 10 μM to 70 μM, T_{max} ascends from 45 °C to 88 °C (Fig. 9e). The calculated η for **11b** is 61%, surpassing most reported organic PTT materials (Fig. S31†).

The photothermal stability of **11a**/**11b** was further examined through multiple heating-cooling cycles (Fig. 9g). Both compounds maintain consistent temperature elevations after five cycles, confirming excellent photostability. The photothermal effect of **11a**/**11b** was also visualized through IR thermal imaging (Fig. 9h), demonstrating a rapid photothermal response. These results highlight the excellent photothermal conversion efficiency and stability of **11a**/**11b**, underscoring their strong potential for PTT applications.

Conclusion

In summary, we have developed a versatile strategy for the synthesis and post-synthetic modulation of hetero-PAHs co-doped with N, O, and S/Se. By integrating acid-catalyzed P–S reactions with thermally induced *ipso*-substitution, we successfully synthesized hetero-PAHs (**3a**/**3b**, **5a**/**5b**, and **7a**/**7b**) featuring chalcogenole, pyran, and pyridine-fused architectures. The systematic expansion of π-conjugation from **3a**/**3b** to **5a**/**5b** and **7a**/**7b** induces a pronounced redshift in both absorption and emission spectra, accompanied by a remarkable enhancement in fluorescence quantum yield (Φ_F) from 4.0% (**3a**) to 30.5% (**7a**).

Beyond structural design, we demonstrate a post-synthetic valence state engineering strategy to precisely modulate photophysical properties. The oxidation of thiophene units into thiophene *S*,*S*-dioxides (**8a** and **9a**) and the methylation of pyridine into pyridinium salts (**11a** and **11b**) significantly alter

electronic structures and intersystem crossing efficiencies. Notably, the introduction of thiophene *S*,*S*-dioxides in **9a** boosts Φ_F to 42.3%, leading to enhanced singlet oxygen ($^1O_2$) generation. Meanwhile, pyridinium-based hetero-PAHs (**11a** and **11b**) show strong near-infrared absorption, accordingly they exhibit excellent photothermal performance, achieving a photothermal conversion efficiency of up to 61%. Furthermore, the superior performance of Se-doped analogs (**7b** and **11b**) over their S-doped counterparts (**7a**, **9a**, and **11a**) in $^1O_2$ generation and/or photothermal conversion underscores the critical role of the heavy-atom effect in optimizing triplet-state dynamics.

This work establishes a facile synthetic blueprint for designing multi-heteroatom-doped PAHs with tunable electronic structures. By leveraging valence state modulation, we unlock new opportunities for tailoring optoelectronic properties, paving the way for applications in organic electronics and phototheranostics.

Data availability

All experimental procedures and characterisation data can be found in the article or in the ESI.†

Author contributions

X. Shao designed the research. Y. Ma and D. Li conducted the synthesis, crystal structure analysis, photophysical measurements; X. Chen and J. Wang carried out the photothermal analysis; X. Hua finished the DFT calculation; C.-S. Yuan, Z. Liu, and H.-L. Zhang provided suggestions for the structural characterizations, optical measurements, and singlet oxygen generation. All authors discussed the results and reviewed the manuscript.

Conflicts of interest

There are no conflicts to declare.

Acknowledgements

This work was supported by National Natural Science Foundation of China (22175080, 22371107, 22161034, 22371151) and The Science and Technology Major Program of Gansu Province of China (22ZD6FA006, 23ZDFA015, 24ZD13FA017).

Notes and references

1 (*a*) C. Wang, H. Dong, W. Hu, Y. Liu and D. Zhu, *Chem. Rev.*, 2012, **112**, 2208–2267; (*b*) A. Narita, X.-Y. Wang, X. Feng and K. Müllen, *Chem. Soc. Rev.*, 2015, **44**, 6616–6643; (*c*) T. C. Pham, V.-N. Nguyen, Y. Choi, S. Lee and J. Yoon, *Chem. Rev.*, 2021, **121**, 13454–13619; (*d*) A. Borissov, Y. K. Maurya, L. Moshniaha, W.-S. Wong, M. Żyła-Karwowska and M. Stępień, *Chem. Rev.*, 2022, **122**, 565–788.

2 (*a*) S. Zhang, W. Guo, J. Wei, C. Li, X.-J. Liang and M. Yin, *ACS Nano*, 2017, **11**, 3797–3805; (*b*) Y. Cai, Z. Wei, C. Song, C. Tang, X. Huang, Q. Hu, X. Dong and W. Han, *Chem. Commun.*, 2019, **55**, 8967–8970; (*c*) C. Ji, W. Cheng, Q. Yuan, K. Müllen and M. Yin, *Acc. Chem. Res.*, 2019, **52**, 2266–2277; (*d*) C. Liu, C. Ji, Z. Fan, R. Ma and M. Yin, *Chem. Commun.*, 2021, **57**, 13126–13129; (*e*) Q. Wang, X. Niu, L. Yang, J. Liu, J. Wang, X. Xu, W. Tang, W. Huang and Q. Fan, *Mater. Chem. Front.*, 2021, **5**, 5689–5697; (*f*) W. Jia, F. Huang, Q. Zhang, L. Zhao, C. Li and Y. Lu, *Chem. Commun.*, 2022, **58**, 6340–6343; (*g*) K. Liu, Z. Jiang, R. A. Lalancette, X. Tang and F. Jäkle, *J. Am. Chem. Soc.*, 2022, **144**, 18908–18917; (*h*) C. Li, G. Jiang, J. Yu, W. Ji, L. Liu, P. Zhang, J. Du, C. Zhan, J. Wang and B. Z. Tang, *Adv. Mater.*, 2023, **35**, 2208229; (*i*) M. Li, Z. Lu, J. Zhang, L. Chen, X. Tang, Q. Jiang, Q. Hu, L. Li, J. Liu and W. Huang, *Adv. Mater.*, 2023, **35**, 2209647; (*j*) Z.-H. Wu, M. Peng, C. Ji, P. Kardasis, I. Tzourtzouklis, M. Baumgarten, H. Wu, T. Basché, G. Floudas, M. Yin and K. Müllen, *J. Am. Chem. Soc.*, 2023, **145**, 26487–26493; (*k*) M. Liang, L. Liu, Y. Sun, J. Li, L. e. Zhang, X. Jiang and W. Wu, *Aggregate*, 2024, **5**, e458; (*l*) X. Liu, B. Chen, M. Wang, X. Gu and L. Zhang, *Angew. Chem., Int. Ed.*, 2025, **64**, e202416160.

3 (*a*) W. Jiang, Y. Li and Z. Wang, *Chem. Soc. Rev.*, 2013, **42**, 6113–6127; (*b*) M. Stępień, E. Gońka, M. Żyła and N. Sprutta, *Chem. Rev.*, 2017, **117**, 3479–3716; (*c*) M. Hirai, N. Tanaka, M. Sakai and S. Yamaguchi, *Chem. Rev.*, 2019, **119**, 8291–8331; (*d*) X.-Y. Wang, X. Yao, A. Narita and K. Müllen, *Acc. Chem. Res.*, 2019, **52**, 2491–2505; (*e*) A. Winter and U. S. Schubert, *Mater. Chem. Front.*, 2019, **3**, 2308–2325; (*f*) W. Wang and X. Shao, *Org. Biomol. Chem.*, 2021, **19**, 101–122.

4 (*a*) J. Wei, B. Han, Q. Guo, X. Shi, W. Wang and N. Wei, *Angew. Chem., Int. Ed.*, 2010, **49**, 8209–8213; (*b*) Z. Liang, Q. Tang, R. Mao, D. Liu, J. Xu and Q. Miao, *Adv. Mater.*, 2011, **23**, 5514–5518; (*c*) Q. Tan, S. Higashibayashi, S. Karanjit and H. Sakurai, *Nat. Commun.*, 2012, **3**, 891; (*d*) U. H. F. Bunz, *Acc. Chem. Res.*, 2015, **48**, 1676–1686; (*e*) S. Ito, Y. Tokimaru and K. Nozaki, *Angew. Chem., Int. Ed.*, 2015, **54**, 7256–7260; (*f*) Q. Tan, H. Chen, H. Xia, B. Liu and B. Xu, *Chem. Commun.*, 2015, **52**, 537–540; (*g*) H. Yokoi, Y. Hiraoka, S. Hiroto, D. Sakamaki, S. Seki and H. Shinokubo, *Nat. Commun.*, 2015, **6**, 8215; (*h*) Y. S. Park, D. J. Dibble, J. Kim, R. C. Lopez, E. Vargas and A. A. Gorodetsky, *Angew. Chem., Int. Ed.*, 2016, **55**, 3352–3355; (*i*) Y. Zhao, Q. Zhang, K. Chen, H. Gao, H. Qi, X. Shi, Y. Han, J. Wei and C. Zhang, *J. Mater. Chem. C*, 2017, **5**, 4293–4301; (*j*) A. Hirono, H. Sakai, S. Kochi, T. Sato and T. Hasobe, *J. Phys. Chem. B*, 2020, **124**, 9921–9930; (*k*) R. K. Dubey, M. Melle-Franco and A. Mateo-Alonso, *J. Am. Chem. Soc.*, 2021, **143**, 6593–6600; (*l*) M. Nishimoto, Y. Uetake, Y. Yakiyama and H. Sakurai, *Chem.–Asian J.*, 2023, **18**, e202201103; (*m*) X.-L. Chen, S.-Q. Yu, J.-Q. Liang, X. Huang and H.-Y. Gong, *Org. Chem. Front.*, 2025, **12**, 1340–1354.

5 O-doped PAHs: (*a*) D. Stassen, N. Demitri and D. Bonifazi, *Angew. Chem., Int. Ed.*, 2016, **55**, 5947–5951; (*b*) T. Miletić, A. Fermi, I. Orfanos, A. Avramopoulos, F. De Leo, N. Demitri, G. Bergamini, P. Ceroni, M. G. Papadopoulos,

S. Couris and D. Bonifazi, *Chem.–Eur. J.*, 2017, **23**, 2363–2378; (*c*) A. Berezin, N. Biot, T. Battisti and D. Bonifazi, *Angew. Chem., Int. Ed.*, 2018, **57**, 8942–8946; (*d*) A. Sciutto, A. Fermi, A. Folli, T. Battisti, J. M. Beames, D. M. Murphy and D. Bonifazi, *Chem.–Eur. J.*, 2018, **24**, 4382–4389; (*e*) S. Dong, T. Y. Gopalakrishna, Y. Han, H. Phan, T. Tao, Y. Ni, G. Liu and C. Chi, *J. Am. Chem. Soc.*, 2019, **141**, 62–66; (*f*) Y. Wang, S. Qiu, S. Xie, L. Zhou, Y. Hong, J. Chang, J. Wu and Z. Zeng, *J. Am. Chem. Soc.*, 2019, **141**, 2169–2176; (*g*) C. M. Wehrmann, R. T. Charlton and M. S. Chen, *J. Am. Chem. Soc.*, 2019, **141**, 3240–3248; (*h*) L. Đorđević, C. Valentini, N. Demitri, C. Mézière, M. Allain, M. Sallé, A. Folli, D. Murphy, S. Mañas-Valero, E. Coronado and D. Bonifazi, *Angew. Chem., Int. Ed.*, 2020, **59**, 4106–4114; (*i*) M. Nishimoto, Y. Uetake, Y. Yakiyama, F. Ishiwari, A. Saeki and H. Sakurai, *J. Org. Chem.*, 2022, **87**, 2508–2519; (*j*) K. Zhang, J. Guo, H. Liu, X. Wang, Y. Yao, K. Yang and Z. Zeng, *Chem. Commun.*, 2023, **59**, 4947–4950.

6 S, Se, or Te doped PAHs: (*a*) H. Ebata, E. Miyazaki, T. Yamamoto and K. Takimiya, *Org. Lett.*, 2007, **9**, 4499–4502; (*b*) C. Mitsui, T. Okamoto, H. Matsui, M. Yamagishi, T. Matsushita, J. Soeda, K. Miwa, H. Sato, A. Yamano, T. Uemura and J. Takeya, *Chem. Mater.*, 2013, **25**, 3952–3956; (*c*) T. Okamoto, C. Mitsui, M. Yamagishi, K. Nakahara, J. Soeda, Y. Hirose, K. Miwa, H. Sato, A. Yamano, T. Matsushita, T. Uemura and J. Takeya, *Adv. Mater.*, 2013, **25**, 6392–6397; (*d*) X. Li, Y. Zhu, J. Shao, B. Wang, S. Zhang, Y. Shao, X. Jin, X. Yao, R. Fang and X. Shao, *Angew. Chem., Int. Ed.*, 2014, **53**, 535–538; (*e*) C. Wang, M. Abbas, G. Wantz, K. Kawabata and K. Takimiya, *J. Mater. Chem. C*, 2020, **8**, 15119–15127; (*f*) T. Guo, Z. Li, L. Bi, L. Fan and P. Zhang, *Tetrahedron*, 2022, **112**, 132752; (*g*) S. Liu, D. Xia, J. Wang, C. Ge, S. Hao, J. Zhang, P. Wang, K. Lin, S. Dong, E. Tretyakov, Y. Yang and X. Gao, *J. Mater. Chem. C*, 2023, **11**, 6089–6094; (*h*) Z. Liu, W. Han, J. Lan, L. Sun, J. Tang, C. Zhang and J. You, *Angew. Chem., Int. Ed.*, 2023, **62**, e202211412.

7 (*a*) D. Wu, W. Pisula, M. C. Haberecht, X. Feng and K. Müllen, *Org. Lett.*, 2009, **11**, 5686–5689; (*b*) S. M. Elbert, M. Reinschmidt, K. Baumgärtner, F. Rominger and M. Mastalerz, *Eur. J. Org Chem.*, 2018, **2018**, 532–536; (*c*) R. Geng, X. Hou, Y. Sun, C. Yan, Y. Wu, H.-L. Zhang and X. Shao, *Mater. Chem. Front.*, 2018, **2**, 1456–1461; (*d*) B. Liu, D. Shi, Y. Yang, D. Liu, M. Li, E. Liu, X. Wang, Q. Zhang, M. Yang, J. Li, X. Shi, W. Wang and J. Wei, *Eur. J. Org Chem.*, 2018, **2018**, 869–873; (*e*) A. Goujon, L. Rocard, H. Melville, T. Cauchy, C. Cabanetos, S. Dabos-Seignon and P. Hudhomme, *J. Mater. Chem. C*, 2022, **10**, 14939–14945; (*f*) C. Valentini, D. Gowland, C. G. Bezzu, D. Romito, N. Demitri, N. Bonini and D. Bonifazi, *Chem. Sci.*, 2022, **13**, 6335–6347; (*g*) A. H. G. David, D. Shymon, H. Melville, L.-A. Accou, A. Gapin, M. Allain, O. Alévêque, M. Force, A. Grosjean, P. Hudhomme, L. L. Bras and A. Goujon, *J. Mater. Chem. C*, 2023, **11**, 14631–14640; (*h*) V. B. S., M. Vadivel, D. P. Singh, V. A. Raghunathan, A. Roy and S. Kumar, *Chem.–Eur. J.*, 2023, **29**, e202300227; (*i*) W. Jiang, H. Zhang, X. Hua, Y. Ma, Y. Feng, C. Yuan, Z. Liu, H.-L. Zhang and X. Shao, *Angew. Chem., Int. Ed.*, 2025, e202500391.

8 (*a*) A. Rodriguez-Serrano, V. Rai-Constapel, M. C. Daza, M. Doerr and C. M. Marian, *Phys. Chem. Chem. Phys.*, 2015, **17**, 11350–11358; (*b*) G. C. Hoover and D. S. Seferos, *Chem. Sci.*, 2019, **10**, 9182–9188; (*c*) M. Santra, M. Owens, G. Birch and M. Bradley, *ACS Appl. Bio Mater.*, 2021, **4**, 8503–8508; (*d*) X. Xia, R. Wang, Y. Hu, Q. Yao, S. Long, W. Sun, J. Fan and X. Peng, *Sci. China:Chem.*, 2022, **65**, 821–828; (*e*) X. Chen, X. Ma, G. Yang, G. Huang, H. Dai, N. Liu and J. Yu, *Nanophotonics*, 2023, **12**, 3645–3652.

9 (*a*) L. Antolini, E. Tedesco, G. Barbarella, L. Favaretto, G. Sotgiu, M. Zambianchi, D. Casarini, G. Gigli and R. Cingolani, *J. Am. Chem. Soc.*, 2000, **122**, 9006–9013; (*b*) G. Barbarella, L. Favaretto, G. Sotgiu, M. Zambianchi, A. Bongini, C. Arbizzani, M. Mastragostino, M. Anni, G. Gigli and R. Cingolani, *J. Am. Chem. Soc.*, 2000, **122**, 11971–11978; (*c*) C.-H. Tsai, D. N. Chirdon, A. B. Maurer, S. Bernhard and K. J. T. Noonan, *Org. Lett.*, 2013, **15**, 5230–5233; (*d*) B. Chen, H. Zhang, W. Luo, H. Nie, R. Hu, A. Qin, Z. Zhao and B. Z. Tang, *J. Mater. Chem. C*, 2017, **5**, 960–968; (*e*) M. K. Etherington, F. Franchello, J. Gibson, T. Northey, J. Santos, J. S. Ward, H. F. Higginbotham, P. Data, A. Kurowska, P. L. Dos Santos, D. R. Graves, A. S. Batsanov, F. B. Dias, M. R. Bryce, T. J. Penfold and A. P. Monkman, *Nat. Commun.*, 2017, **8**, 14987.

10 (*a*) J. E. Cochran, E. Amir, K. Sivanandan, S.-Y. Ku, J. H. Seo, B. A. Collins, J. R. Tumbleston, M. F. Toney, H. Ade, C. J. Hawker and M. L. Chabinyc, *J. Polym. Sci., Part B: Polym. Phys.*, 2013, **51**, 48–56; (*b*) S. Wei, J. Xia, E. J. Dell, Y. Jiang, R. Song, H. Lee, P. Rodenbough, A. L. Briseno and L. M. Campos, *Angew. Chem., Int. Ed.*, 2014, **53**, 1832–1836; (*c*) E. J. Dell, B. Capozzi, J. Xia, L. Venkataraman and L. M. Campos, *Nat. Chem.*, 2015, **7**, 209–214; (*d*) Y. Deng, B. Sun, Y. He, J. Quinn, C. Guo and Y. Li, *Angew. Chem., Int. Ed.*, 2016, **55**, 3459–3462; (*e*) C. Wang, Z. Zhang, S. Pejić, R. Li, M. Fukuto, L. Zhu and G. Sauvé, *Macromolecules*, 2018, **51**, 9368–9381; (*f*) M. Marinelli, A. Candini, F. Monti, A. Boschi, M. Zangoli, E. Salatelli, F. Pierini, M. Lanzi, A. Zanelli, M. Gazzano and F. D. Maria, *J. Mater. Chem. C*, 2021, **9**, 11216–11228; (*g*) S. Jiang, Y. Yu, D. Li, Z. Chen, Y. He, M. Li, G.-X. Yang, W. Qiu, Z. Yang, Y. Gan, J. Lin, Y. Ma and S.-J. Su, *Angew. Chem., Int. Ed.*, 2023, **62**, e202218892.

11 (*a*) D. Wu, L. Zhi, G. J. Bodwell, G. Cui, N. Tsao and K. Müllen, *Angew. Chem., Int. Ed.*, 2007, **46**, 5417–5420; (*b*) J. Fortage, C. Peltier, F. Nastasi, F. Puntoriero, F. Tuyèras, S. Griveau, F. Bedioui, C. Adamo, I. Ciofini, S. Campagna and P. P. Lainé, *J. Am. Chem. Soc.*, 2010, **132**, 16700–16713; (*c*) J. Wang, X. Gu, P. Zhang, X. Huang, X. Zheng, M. Chen, H. Feng, R. T. K. Kwok, J. W. Y. Lam and B. Z. Tang, *J. Am. Chem. Soc.*, 2017, **139**, 16974–16979; (*d*) K. Xu, Y. Fu, Y. Zhou, F. Hennersdorf, P. Machata, I. Vincon, J. J. Weigand, A. A. Popov, R. Berger and X. Feng, *Angew. Chem., Int. Ed.*, 2017, **56**, 15876–15881; (*e*) R. D. Mule, A. C. Shaikh, A. B. Gade and N. T. Patil, *Chem. Commun.*, 2018, **54**, 11909–11912; (*f*) N. Toriumi, N. Asano,

K. Miyamoto, A. Muranaka and M. Uchiyama, *J. Am. Chem. Soc.*, 2018, **140**, 3858–3862; (*g*) P. Karak, S. S. Rana and J. Choudhury, *Chem. Commun.*, 2021, **58**, 133–154; (*h*) Q.-Q. Li, Y. Hamamoto, C. C. H. Tan, H. Sato and S. Ito, *Org. Chem. Front.*, 2022, **9**, 4128–4134; (*i*) Y. Ohno, S. Ando, D. Furusho, R. Hifumi, Y. Nagata, I. Tomita and S. Inagi, *Org. Lett.*, 2023, **25**, 3951–3955; (*j*) L. Huang, Q. Wang, P. Fu, Y. Sun, J. Xu, D. L. Browne and J. Huang, *JACS Au*, 2024, **4**, 1623–1631; (*k*) L. Liu, J. Gong, G. Jiang and J. Wang, *Chem.–Eur. J.*, 2024, **30**, e202400378; (*l*) S. S. Rana, S. Manna and J. Choudhury, *Chem. Commun.*, 2024, **60**, 10942–10945.

12 (*a*) W. Jiang, Y. Li, W. Yue, Y. Zhen, J. Qu and Z. Wang, *Org. Lett.*, 2010, **12**, 228–231; (*b*) M. T. Gabr and F. C. Pigge, *RSC Adv.*, 2015, **5**, 90226–90234; (*c*) J.-W. Chen and C.-C. Chang, *ACS Appl. Mater. Interfaces*, 2016, **8**, 29883–29892; (*d*) X. Gu, E. Zhao, T. Zhao, M. Kang, C. Gui, J. W. Y. Lam, S. Du, M. M. T. Loy and B. Z. Tang, *Adv. Mater.*, 2016, **28**, 5064–5071; (*e*) S. Sowmiah, J. M. S. S. Esperança, L. P. N. Rebelo and C. A. M. Afonso, *Org. Chem. Front.*, 2018, **5**, 453–493; (*f*) Y. Gao, X. Wang, X. He, Z. He, X. Yang, S. Tian, F. Meng, D. Ding, L. Luo and B. Z. Tang, *Adv. Funct. Mater.*, 2019, **29**, 1902673; (*g*) M. Imran, C. M. Wehrmann and M. S. Chen, *J. Am. Chem. Soc.*, 2020, **142**, 38–43; (*h*) Q. Wan, R. Zhang, Z. Zhuang, Y. Li, Y. Huang, Z. Wang, W. Zhang, J. Hou and B. Z. Tang, *Adv. Funct. Mater.*, 2020, **30**, 2002057; (*i*) C. M. Wehrmann, M. Imran, C. Pointer, L. A. Fredin, E. R. Young and M. S. Chen, *Chem. Sci.*, 2020, **11**, 10212–10219; (*j*) Z. Liu, Q. Wang, W. Qiu, Y. Lyu, Z. Zhu, X. Zhao and W.-H. Zhu, *Chem. Sci.*, 2022, **13**, 3599–3608; (*k*) L. Wang, L. Qi, Q. Zhang, B. Xue, Z. Zheng, P. Yin, Y. Xue, W. Yang and Y. Li, *Chem. Sci.*, 2023, **14**, 4612–4619; (*l*) Q.-L. Zhang, Q.-T. Fan, Y. Zhou, J. Zhang and F.-L. Zhang, *Org. Chem. Front.*, 2024, **11**, 2884–2890.

13 (*a*) E. D. Cox and J. M. Cook, *Chem. Rev.*, 1995, **95**, 1797–1842; (*b*) A. K. Mandadapu, M. Saifuddin, P. K. Agarwal and B. Kundu, *Org. Biomol. Chem.*, 2009, **7**, 2796.

14 (*a*) X. Hou, Y. Zhu, Y. Qin, L. Chen, X. Li, H.-L. Zhang, W. Xu, D. Zhu and X. Shao, *Chem. Commun.*, 2017, **53**, 1546–1549; (*b*) W. Wang, L. Feng, X. Hua, C. Yuan and X. Shao, *Chin. J. Chem.*, 2021, **39**, 3413–3420.

15 T. Fukaminato, T. Hirose, T. Doi, M. Hazama, K. Matsuda and M. Irie, *J. Am. Chem. Soc.*, 2014, **136**, 17145–17154.

16 (*a*) S. Liu, Y. Li, H. Zhang, Z. Zhao, X. Lu, J. W. Y. Lam and B. Z. Tang, *ACS Mater. Lett.*, 2019, **1**, 425–431; (*b*) S. Furukawa, J. Wu, M. Koyama, K. Hayashi, N. Hoshino, T. Takeda, Y. Suzuki, J. Kawamata, M. Saito and T. Akutagawa, *Nat. Commun.*, 2021, **12**, 768; (*c*) Y. Li, X. Fan, Y. Li, S. Liu, C. Chuah, Y. Tang, R. T. K. Kwok, J. W. Y. Lam, X. Lu, J. Qian and B. Z. Tang, *ACS Nano*, 2022, **16**, 3323–3331.

17 (*a*) W. Fan, B. Yung, P. Huang and X. Chen, *Chem. Rev.*, 2017, **117**, 13566–13638; (*b*) G. Feng, G.-Q. Zhang and D. Ding, *Chem. Soc. Rev.*, 2020, **49**, 8179–8234; (*c*) Q. Xie, J. Tang, S. Guo, Q. Zhao and S. Li, *Molecules*, 2023, **28**, 6038; (*d*) D. Ma, H. Bian, M. Gu, L. Wang, X. Chen and X. Peng, *Coord. Chem. Rev.*, 2024, **505**, 215677.

18 (*a*) S. Liu, G. Feng, B. Z. Tang and B. Liu, *Chem. Sci.*, 2021, **12**, 6488–6506; (*b*) W. Fan, P. Huang and X. Chen, *Chem. Soc. Rev.*, 2016, **45**, 6488–6519; (*c*) X. Zhao, J. Liu, J. Fan, H. Chao and X. Peng, *Chem. Soc. Rev.*, 2021, **50**, 4185–4219.

19 (*a*) K. Wen, H. Tan, Q. Peng, H. Chen, H. Ma, L. Wang, A. Peng, Q. Shi, X. Cai and H. Huang, *Adv. Mater.*, 2022, **34**, 2108146; (*b*) S. Yao, Y. Chen, W. Ding, F. Xu, Z. Liu, Y. Li, Y. Wu, S. Li, W. He and Z. Guo, *Chem. Sci.*, 2023, **14**, 1234–1243.

20 (*a*) K. C. Park, J. Cho and C. Y. Lee, *RSC Adv.*, 2016, **6**, 75478–75481; (*b*) F. Xu, H. Li, Q. Yao, H. Ge, J. Fan, W. Sun, J. Wang and X. Peng, *Chem. Sci.*, 2019, **10**, 10586–10594; (*c*) Q. Xu, Y. Gao, X. Wu, H. Hang, H. Li, Y. Chen, W. Wang and H. Tong, *New J. Chem.*, 2019, **43**, 16385–16390; (*d*) H. Bian, D. Ma, F. Pan, X. Zhang, K. Xin, X. Zhang, Y. Yang, X. Peng and Y. Xiao, *J. Am. Chem. Soc.*, 2022, **144**, 22562–22573; (*e*) W. Cao, Y. Zhu, F. Wu, Y. Tian, Z. Chen, W. Xu, S. Liu, T. Liu and H. Xiong, *Small*, 2022, **18**, 2204851; (*f*) W.-X. Wang, J.-J. Chao, Z.-Q. Wang, T. Liu, G.-J. Mao, B. Yang and C.-Y. Li, *Adv. Healthcare Mater.*, 2023, **12**, 2301230.

21 R. Englman and J. Jortner, *Mol. Phys.*, 1970, **18**, 145–164.

22 F.-Z. Xu, L. Zhu, H.-H. Han, J.-W. Zou, Y. Zang, J. Li, T. D. James, X.-P. He and C.-Y. Wang, *Chem. Sci.*, 2022, **13**, 9373–9380.

23 (*a*) R.-L. Ge, P.-N. Yan, Y. Liu, Z.-S. Li, S.-Q. Shen and Y. Yu, *Adv. Funct. Mater.*, 2023, **33**, 2301138; (*b*) H. S. Jung, P. Verwilst, A. Sharma, J. Shin, J. L. Sessler and J. S. Kim, *Chem. Soc. Rev.*, 2018, **47**, 2280–2297; (*c*) B. Lu, Y. Huang, Z. Zhang, H. Quan and Y. Yao, *Mater. Chem. Front.*, 2022, **6**, 2968–2993; (*d*) Z. Zhao, C. Chen, W. Wu, F. Wang, L. Du, X. Zhang, Y. Xiong, X. He, Y. Cai, R. T. K. Kwok, J. W. Y. Lam, X. Gao, P. Sun, D. L. Phillips, D. Ding and B. Z. Tang, *Nat. Commun.*, 2019, **10**, 768.

24 (*a*) S. Li, Q. Deng, Y. Zhang, X. Li, G. Wen, X. Cui, Y. Wan, Y. Huang, J. Chen, Z. Liu, L. Wang and C.-S. Lee, *Adv. Mater.*, 2020, **32**, 2001146; (*b*) X. Chen, X. Ma, G. Yang, G. Huang, H. Dai, J. Yu and N. Liu, *ACS Appl. Mater. Interfaces*, 2024, **16**, 12332–12338; (*c*) M. Li, Z. Lu, J. Zhang, L. Chen, X. Tang, Q. Jiang, Q. Hu, L. Li, J. Liu and W. Huang, *Adv. Mater.*, 2023, **35**, 2209647; (*d*) L. Feng, C. Li, L. Liu, X. Chen, G. Jiang, J. Wang and B. Z. Tang, *Angew. Chem., Int. Ed.*, 2022, **61**, e202212673; (*e*) H. Gu, W. Liu, W. Sun, J. Du, J. Fan and X. Peng, *Chem. Sci.*, 2022, **13**, 9719–9726.

25 (*a*) D. K. Roper, W. Ahn and M. Hoepfner, *J. Phys. Chem. C*, 2007, **111**, 3636–3641; (*b*) R. Marin, A. Skripka, L. V. Besteiro, A. Benayas, Z. Wang, A. O. Govorov, P. Canton and F. Vetrone, *Small*, 2018, **14**, 1803282.